Synthesis and characterization of UV-curable nanocellulose/ZnO/AlN acrylic flexible films: thermal, dynamic mechanical and piezoelectric response

Synthesis and characterization of UV-curable nanocellulose/ZnO/AlN acrylic flexible films: thermal, dynamic-mechanical and piezoelectric response

M. A. Signore[1], C. De Pascali[1], D. Duraccio[2,3], G. Malucelli[2], A. Fioravanti[4], E. Melissano[1], M. C. Martucci[1], M. Masieri[5], P. Siciliano[1], L. Francioso[1*]

[1]*CNR, Institute for Microelectronics and Microsystems, Via Monteroni, 73100 Lecce, Italy*

[2]*Dipartimento di Scienza Applicata e Tecnologia, Politecnico di Torino, Viale T. Michel 5, 15121 Alessandria, Italy*

[3]*Istituto per le Macchine Agricole e Movimento Terra (IMAMOTER)-UOS di Torino, Consiglio Nazionale delle Ricerche , Strada delle Cacce 73, 10135 Torino, Italy*

[4] *Istituto per le Macchine Agricole e Movimento Terra, Consiglio Nazionale delle Ricerche, Via Canal Bianco 28, 44124 Ferrara, Italy*

[5]*CNR, Institute for Archaeological and Monumental Heritages, Via Monteroni, 73100 Lecce, Italy*

** Corresponding author email: lucanunzio.francioso@cnr.it*

ABSTRACT

This work demonstrates a simple route to fabricate nanocomposites based on ZnO nanostructures and nanocellulose dispersed in a UV-cured acrylic matrix (EC) for application as functional coatings for self-powered applications. Morphological, thermal and dynamic-mechanical properties of the nanocomposites were characterized by XRD, SEM and DSC. The piezoelectric behavior was evaluated in terms of Root Mean Square open-circuit voltage, at different accelerations applied to cantiveler beams. The generated voltage was correlated with ZnO nanostructures morphology, aluminum nitride film integration on the beam and proof mass insertion at the tip. Nitride layer increased the RMS voltage from 1-2.4 mV up to 3.9 mV (using ZnO-nanoflowers). As confirmed by

XRD analyses, ZnO nanostructures into the acrylic matrix favored an ordered structural arrangement of the deposited AlN layer, hence improving nanocomposites piezoelectric response. With proof mass insertion, the output voltage was further increased, up to 4.5 mV for the AlN-coated system containing ZnO nanoflowers.

INTRODUCTION

Piezoelectric materials have the capability to convert mechanical strain energy into electrical potential, and vice versa. This extraordinary physical feature favors their employment in many fields of application, particularly those related to voltage generation from mechanical vibrations [1]. In this context, many researchers have recognized that ambient vibration is a very attractive source of energy, being ubiquitous and easily accessible, and supplying energy densities estimated in the range from 50 to 250 $\mu W/cm^3$. For this reason, one of the most investigated and exploited property of the piezoelectric materials is their capability to harvest mechanical energy (usually from ambient vibration) in the form of electrical energy for the powering of electronic devices. Nowadays, the scientific research is focused, on one hand, on developing devices able to efficiently exploit renewable energy sources and, on the other hand, on encouraging the use of environmentally-friendly materials as a sustainable alternative to the traditional ones [2, 3, 4]. Piezoelectric materials fulfill these requirements because, in addition to their utilization as renewable energy sources, they can be deposited on flexible substrates and show cost-effective scalability, which are key elements for innovative devices in the field of green technologies [5]. Among the large variety of solutions aimed at fabricating new flexible piezoelectric materials, composites comprised of piezoelectric ceramic fillers embedded within a polymeric matrix have been proposed. In this frame, UV curable systems have been considered as a particularly suitable matrix to implement new smart composites thanks to their rapid cure and wide range of

properties [6]. UV-curing represents a more economic, faster and nontoxic method than the other curing processes. Besides, compared to conventional coating techniques, it does not require the use of any solvent, hence reducing volatile compounds emission and resulting environmentally-friendly [7]. The UV-cured systems show flexibility, biocompatibility, easiness of processing large areas, simple integration into devices, reduction of device size, improved device reliability, and lower production costs [8]. By tailoring the physical properties and the morphology of the embedded piezoelectric, according to the specific application [9], the number of available composite materials and device designs can be remarkably increased [10]. Several works have been reported in literature about the synthesis of piezoelectric composites for power generation. As examples, a flexible piezoelectric nanocomposite consisting of zinc oxide (ZnO) nanostructures embedded in a cellulose matrix was presented in [11] but vibrational tests did not report the voltage signals; Mahadeva et al. [12] developed hybrid piezoelectric paper anchoring nanostructured barium titanate ($BaTiO_3$); electrospun polyacrylonitrite (PAN) fibers containing SbSI nanowires were synthesized to build a piezoelectric generator [13], but the deposition technique suffered the lack of future microfabrication process scale-up; PZT-epoxy-multiwalled carbon nanotube (MWCNT) nanocomposites were fabricated by keeping constant the volume fraction of PZT and varying MWCNT loading for investigating the piezoelectric response [14]; Singh et al. prepared nanocomposites made of a PVDF matrix filled with BaTiO3 nanoparticles and studied their piezoelectric behavior [15]. Recently, nanocellulose has gained great interest among the combinations of materials that can be exploited to fabricate nanocomposites [16]. In spite of its low piezoelectricity, it is often preferred to other piezoelectric fillers with the higher piezoelectric response, because of its abundance, low production cost, biodegradability and no industrial waste and environmental pollution [17]. For these reasons, new ways to improve nanocellulose piezoelectricity are being investigated, by exploiting suitable chemical or mechanical

appropriate treatments [18]. The combination of nanocellulose and zinc oxide (ZnO) nanostructures has been considered a promising way for the fabrication of self-powered nanogenerators, as reported in literature [19, 20, 21, 22]. In addition to the nanocellulose advantages, ZnO exhibits interesting complementary properties. It is a semiconductor material with a wide band gap (3.37 eV) and high electron-hole binding energy (60 meV), largely used in electronic, optical, laser and LED devices [23]. Apart from its well-known piezoelectric properties, it is biocompatible, hence it can be used in human and environmentally-friendly biomedical engineering systems and green energy production devices.

Motivated by the promising results obtained in a previous work [24], a new piezoelectric polymeric composite was developed. In particular, in this work, the structural, morphological and piezoelectric properties of new UV-curable systems containing piezoelectric fillers, i.e. cellulose nanocrystals (CNCs) alone or in combination with ZnO nanostructures, embedded into an acrylic UV-curable matrix, are thoroughly investigated. The piezoelectric response of the prepared composites was evaluated by integrating these materials onto rectangular cantilever beams, free on three edges and clamped on a short edge, with 100 nm-thick Al films, sputtered on the top and bottom surfaces, working as electrical contacts. The fabricated cantilever demonstrates that all the studied systems are compatible with thin film vacuum deposition processes, so upscaling to the large area processing will be very easy. With the aim to improve the piezoelectric generation of the nanocomposites, the integration of a PVD AlN layer onto top surface of the beam and the anchoring of a proof mass on the beam tip was also evaluated. To this aim, the Root Mean Square (RMS) open circuit output voltage of all devices was recorded at different applied accelerations.

EXPERIMENTAL

Preparation of the nanocomposite films

The freeze-dried cellulose nanocrystal (CNC) powder was provided by CelluloseLab (Canada). Before use, it was ground in a mortar in order to obtain a uniform powder dimension. The selected ZnO nanostructures (i.e. nanoflowers and nanoneedles) were prepared through wet chemistry processes as previously described [25]. In brief, nanoflowers (hereinafter coded as ZnF) were prepared heating a water solution 0.05 M of $Zn(NO_3)_2 \bullet 6H_2O$ at 60 °C then adding a proper amount of ammonium hydroxide (28 %, Carlo Erba Reagents) to reach a pH of 10. After 30 min of thermal treatment at 60 °C, the ZnO precipitate was filtered, repeatedly washed with water and diethyl ether, then dried at 100 °C in air overnight. Nanoneedles (hereinafter coded as ZnN) were obtained adding a proper amount of ammonium hydroxide (28 %, Carlo Erba Reagents) to a water solution 0.05 M of $Zn(NO_3)_2 \bullet 6H_2O$, bringing the solution pH to 10. The mixture was then kept at 95 °C and for 7 hours to obtain short, long and irregular needles respectively. The precipitate was filtered, washed several times with water and diethyl ether, before drying at 100 °C in air overnight in an oven. Commercial bis-phenol A ethoxylate diacrylate (Ebecryl 150, hereinafter coded as EB), kindly supplied by Cytec Industries BV (Netherlands) and 4% wt. of photoinitiator (Irgacure 1173, namely 2,2-dimethyl-2-hydroxy acetophenone, from BASF, Italy) were used for preparing the acrylic UV-curable mixture; then, CNCs with and without ZnO nanofillers were dispersed in the curable precursor at 4 wt.% and ultrasonicated for 30 min at room temperature. The obtained dispersions were coated on glass slides, using a wire wound applicator (nominal film thickness: 200 µm) and then exposed to the UV radiation provided by a F300 S apparatus (Heraeus Noblelight, USA) working in static conditions. The radiation intensity on the sample surface, measured with an UV-meter, was about 800 mW/cm^2; two not consecutive exposures of 15 s were employed for completing the photopolymerization reaction. Three types of nanocomposite films

were prepared: one type contains 4 wt.% cellulose nanocrystals (hereinafter coded as EC); the other two nanocomposite films contain 2 wt.% cellulose nanocrystals and 2 wt.% ZnO nanostructures embedded in the acrylic resin. In particular, the films incorporating ZnO flowers or ZnO needles are hereinafter coded as EC-ZnF or EC-ZnN, respectively. A second set of these nanocomposites was obtained by modifying the previous ones with the deposition of an AlN layer on the top surface. The nitride film (600 nm-thick), deposited by sputtering, was added with the aim to investigate the preferential growth direction on the polymer foil and the obtainable enhancement in terms of piezoelectric response of the overall structure. Hereinafter, the samples belonging to this second set will be coded as EC+AlN, EC-ZnN+AlN, EC-ZnF+AlN.

Structural and morphological characterization: XRD and SEM analyses

All samples were structurally characterized by X-ray diffraction (XRD) measurements by using the Cu-Kα radiation over the range 2θ = 10°-60° with step of 0.02° and 100 s dwell time. Neglecting the microstrain, the crystallite sizes (D) of the thin films were obtained from the Debye-Scherrer formula:

$$D = \frac{K\lambda}{\beta cos\theta} \qquad (1)$$

where K is the shape factor of the average crystallite with value of 0.94, λ the X-ray wavelength (0.15406 nm for Cu target), β the full width at half maximum (FWHM) of the peak in radians, θ the Bragg angle. The texture coefficient T_c(*hkl*) of the (*hkl*) plane defined by Barret and Massalski was employed for describing the preferred orientation:

$$Tc(hkl) = \frac{\frac{I(hkl)}{I_0(hkl)}}{\frac{1}{N}\sum_N \frac{I(hkl)}{I_0(hkl)}} \qquad (2)$$

where T_c(*hkl*) is the texture coefficient of the (*hkl*) plane, *I(hkl)* the measured intensity, I_0(hkl) the

ASTM standard intensity of the corresponding powder, and N is the reflection number of significant peaks. From this definition, it is clear that the deviation of the texture coefficient from unit implies the preferred orientation of the growth: the larger of texture coefficient deviates from unit, the higher will be the preferred orientation of the film.

FESEM analyses were performed on the UV-cured films coated with the AlN layer. To this aim, a Zeiss Merlin apparatus was employed. Before carrying out the analyses, the samples were metallized, depositing a 50 nm coating of Pt. Al electrode surface deposited on AlN thin film was observed by means of a Scanning Electron Microscope (SEM, Zeiss Evo 50 XVP with). SEM observations were performed at room temperature, high vacuum mode and with an acceleration voltage of 20 kV.

Thermal and dynamic-mechanical characterization

DSC measurements were performed by using a Mettler DSC-822 instrument according to the following cycle: (1) heating from 0 °C to 160 °C at 10 °C/min; (2) cooling down to 0 °C at -10 °C/min; and (3) heating from 0 °C to 160 °C at 10 °C/min. The glass transition temperature (Tg) was taken at the midpoint of heat capacity changes. Calibration was performed using indium as standard (Tm = 156.4 °C; ΔHm = 28.15 J/g). TG/dTG analyses were performed using a TA Q500 thermo balance (TA Instruments) (experimental error: ± 0.5% wt., ±1 °C) with a heating rate of 10°C/min from 30 to 700 °C. The samples (ca. 20 mg) were placed in open alumina pans and fluxed with air (gas flow: 60 ml/ min). $T_{10\%}$ (temperature, at which 10% weight loss occurs) and Tmax (temperature, at which maximum weight loss rate is achieved) were evaluated, as well as the residue at 700°C. The viscoelastic properties of samples were measured using a DMA Q800 (TA Instruments). The experiments were performed in tensile configuration with a heating rate of 3 °C/min, from 30 °C to 150 °C. These tests were carried out at a constant frequency of 1 Hz and

0.05 % of oscillation amplitude in strain-controlled mode. The storage modulus (G'), loss modulus (G") and tanδ curve were recorded. Tg values were calculated from the peak value of tanδ curve. For each formulation, the tests were repeated three times and the experimental error was calculated as the standard deviation for all the measured parameters.

Evaluation of the piezoelectric open circuit voltage generated by the composites

Rectangular cantilevers with a footprint area of about 20 × 15 mm^2 were fabricated starting from the two sets of UV-cured nanocomposite films (with and without AlN layer), and they were used for piezoelectric measurements; 100 nm-thick aluminum thin films were deposited on both sides by RF sputtering onto a 10 × 10 mm^2 area (active area), working as electrodes for the collection of the generated charges. The AlN film of the second set of samples was deposited onto the top side of the cantilever, before the electrode deposition.

The experimental set-up for assessing the piezoelectric response of the samples consisted of a sinusoidal signal generator connected to a PCB Piezotronic 2100E power amplifier to drive the electromechanical shaker (mod. 2007E from the same producer), a GW-Instek GDS2204200 MHz 4 channel DSO (digital storage oscilloscope) and a commercial reference accelerometer. The fabricated beams were mounted on the shaker and the Al electrodes were connected to the DSO for signals collection, using 100 µm diameter pure gold wires connected to 10X probes; a commercial reference accelerometer (mod. PCB 352CSS with charge amplifier) was bonded on the topside of the oscillating plate (to precisely evaluate the maximum acceleration provided to the tested devices). The DSO was exploited for recording the output signal from each device, together with the signal of the reference accelerometer. All the devices were examined at their resonance frequency and three different acceleration values (namely, 5, 7 and 10 g).

In order to increase the output voltage signal, thanks to a more effective beam bending, a square-shaped iron tip mass of 0.55 g with a surface area of 25 mm^2 and a thickness of 0.5 mm, was added to the free end of all the cantilevers coated with the AlN layer. The experimental error of the output voltage was equal to about 0.02 mV.

RESULTS AND DISCUSSION

XRD and SEM analyses

Figure 1 shows the θ–2θ measurement performed on CNC powder before its dispersion into the acrylic resin.

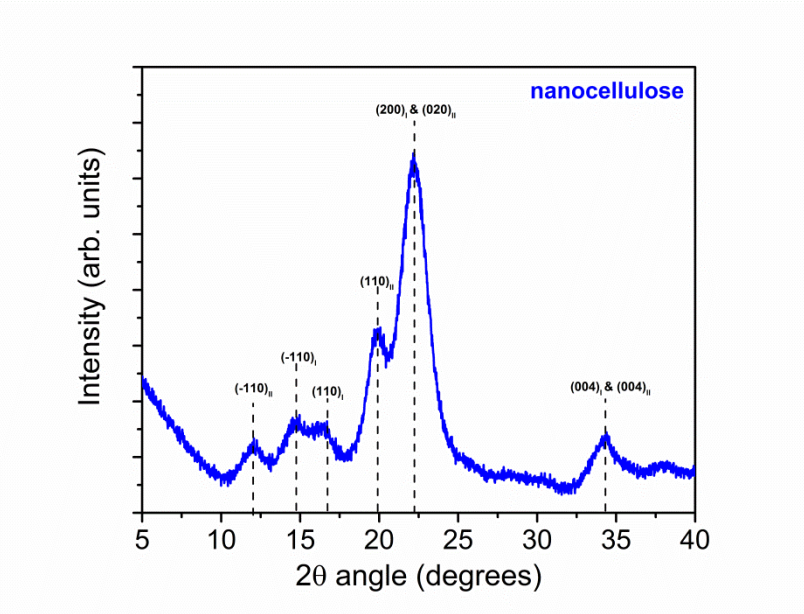

FIGURE 1. XRD spectrum of commercial CNC.

Depending on the orientation of the hydroxyl groups in the structure, cellulose in its solid state can be found with areas of high crystallinity and amorphous regions. Different crystalline structures of cellulose exist, namely cellulose I, II, III, IV and V. Cellulose I and II are the most studied forms [25]. Generally, commercial nanocellulose can have a mixed content of amorphous

and cellulose I and II crystalline phases, as observed in the spectrum of Figure 1, where the phases (I and II) are indicated as subscript.

The structural analyses of the samples with ZnO nanostructures (needles or flowers) dispersed in the acrylic matrix containing cellulose nanocrystals, with and without the AlN layer, are displayed in Figure 2.

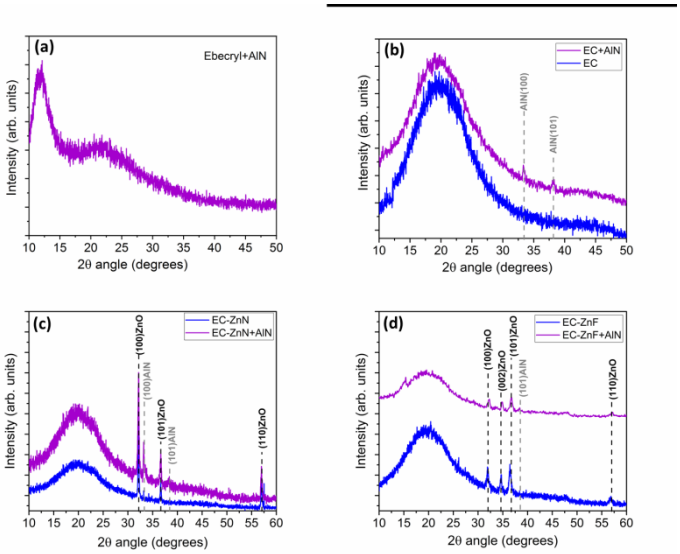

FIGURE 2. XRD spectra of all the analyzed samples: 2a) XRD spectrum of the pure acrylic matrix with AlN 600 nm-thick deposited; 2b) comparison of XRD spectra of the pure acrylic matrix (EC) with EC+AlN 600 nm-thick deposited; 2c) comparison of XRD spectra of the EC+nanoneedles with EC+nanoneedles+AlN; 2d) comparison of XRD spectra of the EC+nanoflowers with EC+nanoflowers+AlN.

Figure 2a shows the XRD spectrum of the pure acrylic matrix with a layer of AlN 600 nm-thick deposited on one surface. The sample appears rather amorphous and no AlN peaks are detected. Figure 2b depicts the comparison of XRD spectra of EC with EC/AlN 600 nm-thick; Figure 2c shows the XRD spectra of the EC/nanoneedles (EC-ZnN) with EC/nanoneedles/AlN (EC-ZnN+AlN); finally Figure 2c reports the comparison of XRD spectra of the EC/nanoflowers (EC-ZnF) with EC/nanoflowers/AlN (EC-ZnF+AlN). In all the spectra, a broad peak (halo) appears in the range θ-2θ= 10-30°, attributable to amorphous resin that probably hides the weak peaks of nanocellulose, being CNC dispersed at a very low concentration (2 wt. %). XRD spectrum of EC+AlN sample (Figure 2b) reveals the presence of two weak peaks, attributable to AlN(100) at 2θ= 33.3° and to

AlN(101) at 2θ= 38.1°. The texture coefficient Tc(100) = 1.1 indicates a slight preferential orientation along (100) with respect to (101) planes being Tc(101) = 0.98. According to equation (1), the grain size along the preferential growth direction, i.e. (100), is about 33.3 nm. Figure 2c shows the XRD spectra of the EC-ZnN samples. Besides the broad halo attributable to the acrylic matrix, peaks referring to ZnO are present. In particular, ZnO(100) at 2θ = 32.1° is the strongest peak observed in the samples, with texture coefficient Tc(100) = 1.58 that confirms the preferential orientation along this plane; other peaks such as (101) at 2θ= 36.5° and (110) at 2θ= 56.8° have substantially lower intensities and texture coefficients equals to Tc(101)= 0.41 and Tc(110) = 1.01.

When the AlN layer is deposited on the surface of the film containing CNC and ZnO needles (EC-ZnN+AlN sample), AlN(100) and AlN(101) peaks are detected at 2θ= 33.2° and 38°, respectively. AlN film grows along the crystallographic planes of ZnO dispersed into the resin, being preferentially oriented along (100) planes with T*c*(100) = 1.22 with respect to T*c*(101) = 0.78. The grains size along the preferential growth direction is equal to about 62 nm, while the grains size oriented along (101) planes is about 20 nm. Figure 2d depicts the structural arrangement of ZnO flowers dispersed into EC based-resin, with and without the AlN layer. This sample shows four diffraction peaks at 2θ= 32°, 34,6°, 36.7° and 56.7°, attributable to reflections from (100), (002), (101) and (110) planes of ZnO. A preferential orientation along (002) direction with T*c*=1.22 was observed. Unlike ZnO needles, where the AlN layer grows with a certain structural order following the orientation of the underlying ZnO nanostructures, only a very weak and wide peak attributable to AlN(101) appears at 2θ= 37.8°, with a resulting grain size of about 8 nm. Figure 3 shows SEM images of the investigated nanostructures.

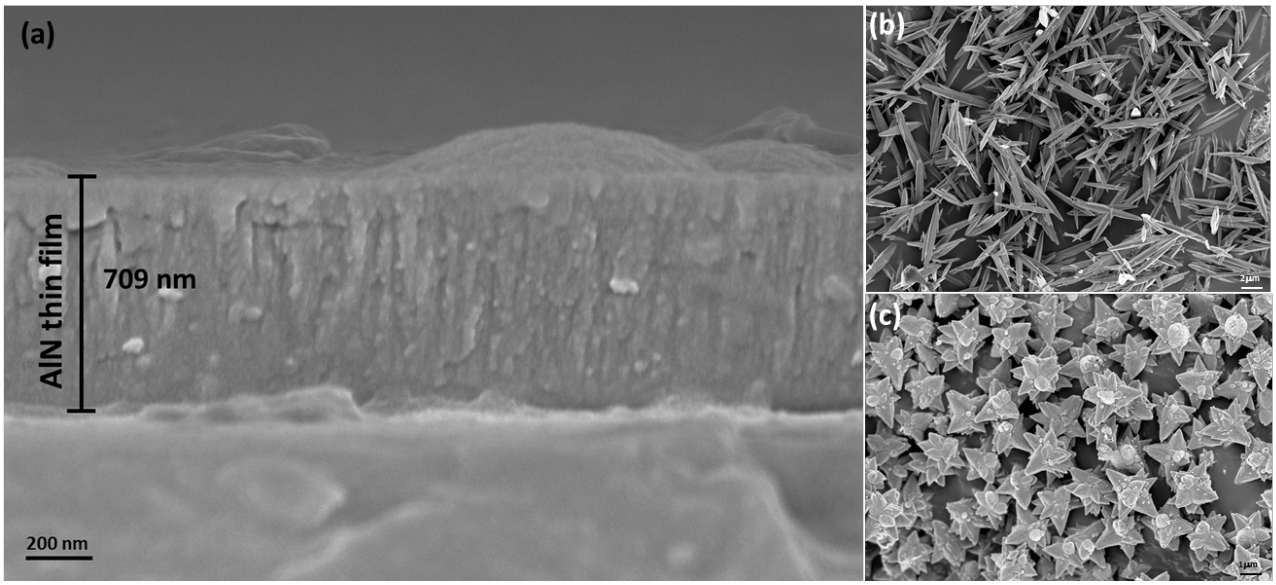

FIGURE 3. (a) SEM cross section of EC-ZnN+AlN sample; (b) ZnO nanoneedles and (c) ZnO nanoflowers surface morphologies.

In particular, Figure 3a represents FESEM cross-sectional image of EC-ZnN+Al sample, taken as representative: the AlN microstructure is typical, with very densely packed columnar grains, the surface morphology is not very smooth and the evaluated thickness is compatible with that of the deposited AlN/Al bilayer. Figures 3b and 3c depict the surface morphologies of the as-deposited ZnO nanostructures, needle and flowers, respectively, before there dispersion in the acrylic matrix.

Summarizing, the AlN film deposited on unfilled UV-cured EB grows in amorphous form. The presence of nanostructures dispersed into the matrix favors a more ordered film arrangement. In particular, the nitride deposited on EC composite grows along (100) and (101) planes with very similar peak intensities. When the resin is loaded with ZnO needle nanostructures, the AlN film exhibits a preferential (100) growth direction, following the preferential texture of ZnO, which seems to force the nitride film to arrange along the same crystallographic orientation. On the contrary, ZnO flowers nanostructures show a more polycrystalline structural organization, which does not favor any preferential growth orientation of the AlN film. Besides, as it is known that the

(002) directions have the lowest energy hexagonal closed packed (HCP) plane in the AlN system, the results clearly indicate that the system is far from the lowest energy state, which can be reached by a suitable tuning of the sputtering deposition parameters.

Thermal and dynamic-mechanical analyses

Figure 4 shows the first and second heating up DSC runs for EC, EC-ZnF and EC-ZnN films. In the first run, the relaxation enthalpy, superimposed to the specific heat changes associated with the glass transition of the polymer network, is present in all the analyzed films.

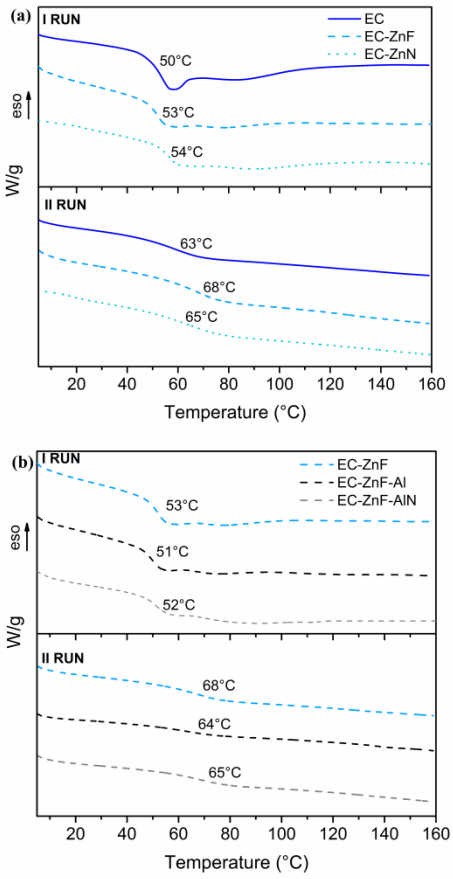

FIGURE 4. DSC thermograms of the UV-cured nanocomposites: (a) before sputtering deposition of AlN and Al electrode for all samples and (b) after the sputtering deposition of nitride and metallic layers for ZnF sample taken as representative.

This finding, as already reported [24], is attributable to the fast UV-curing process that freezes the macromolecules in a non-equilibrium thermodynamic state. The absence of exothermic

phenomena above the glass transition confirms that the conditions adopted for the photo-polymerization process (i.e. radiation intensity, number of exposures to UV radiation, duration of each exposure) are enough for promoting the formation of a fully cured network, also in the presence of the CNC and ZnO nanofillers. In the second run, the relaxation enthalpy disappears because the free macromolecules segments between cross-link points can re-arrange in a more stable conformational structure as a consequence of the heating at temperatures beyond the glass transition and the subsequent cooling down. Besides, the Tg values, reported in Figure 4, show an increase of the glass transition temperature of EC-ZnF and EC-ZnN with respect to that of EC system. This increase, which is more evident in the second run, indicates that the nanofillers (ZnF and ZnN) interact with the polymer segments, somehow limiting the mobility of these latter [26]. In order to assess whether the temperature reached during the sputtering processes of Al and AlN (about 80 °C as verified by a thermocouple placed near the substrate) may favor some changes of the structure of the polymer network, DSC runs were performed on the cantilever surface that had not been coated by Al electrodes for EC and EC-ZnO systems. As an example, Figure 4b collects the first and second heating up runs for EC-ZnF, EC-ZnF-AlN (with and without Al). The curves of the first run show relaxation enthalpy and Tg values pretty similar to that of untreated EC-ZnF. Analogously, in the second run, as already observed, only the Tg steps are visible and are slightly higher with respect to the unfilled UV-cured film. This finding confirms that the sputtering process with Al does not induce any modification in the polymer network. Figure 5 shows the TG and dTG curves for EC-ZnO composite films. T10% and Tmax, i.e. the temperatures corresponding to a 10% weight loss and at the maximum of the derivative curves, respectively, are listed in Table 1, as well as the final residue at 700 °C.

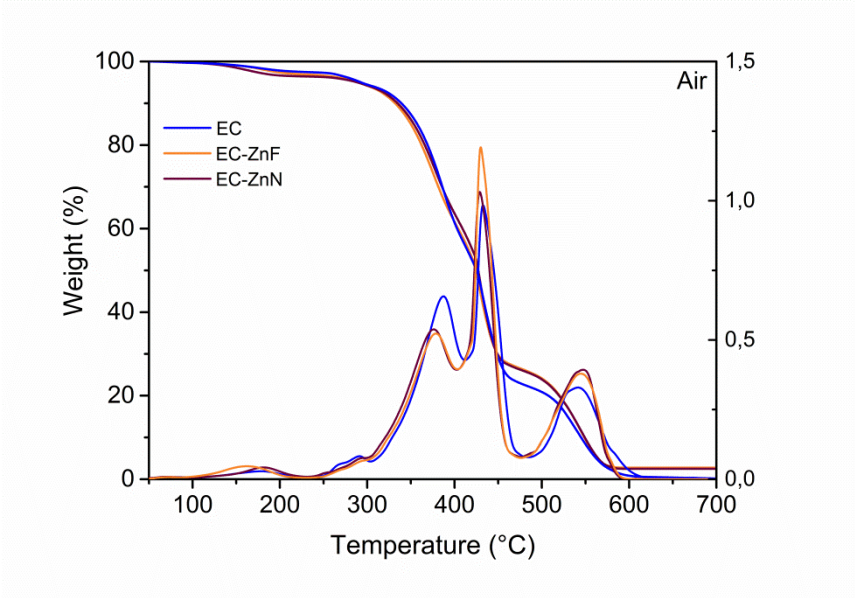

FIGURE 5. Tg and dTg curves of ZnO composites in air.

	T10% (°C)	Tmax1 (°C)	Residue @ Tmax1 (%)	Tmax2 (°C)	Residue @ Tmax2 (%)	Tmax3 (°C)	Residue @ Tmax3 (%)	Residue @ 700°C (%)
EC	331	387	69	433	43	543	11	0.3
EC-ZnF	333	378	72	429	45	547	11	2.6
EC-ZnN	332	376	75	430	46	546	11	2.6

TABLE 1. Thermogravimetric data of EB/ZnO composite films in air.

All the curves appear very similar and show three main degradation steps: the first step, in the range between 300 and 400 °C, could be ascribed to the degradation of low molecular weight structures, the second one in the range between 400 and 500 °C refers to the main degradation of the polymer network, while the last one (from 500 to 600 °C) can be attributed to the further oxidation of the degradation products formed during the previous steps. Whatever the fillers

morphology is, the thermal stability of EC-ZnO nanocomposites at low temperatures is comparable to that of EC. T10% values are about 332 °C for all the nanocomposites. Their Tmax values of the first two degradation step are lower than that of EC film. Conversely, the Tmax of the last degradation step is slightly higher than that of EC film. In addition, the nanocomposites dTg curves are sharper as compared to that of EC, indicating that the ZnO nanostructures accelerate the polymer degradation steps. The storage modulus (logG'), the loss modulus (logG") and tanδ as a function of temperature for the EC-ZnF and EC-ZnN are compared with those of EC in Figure 6.

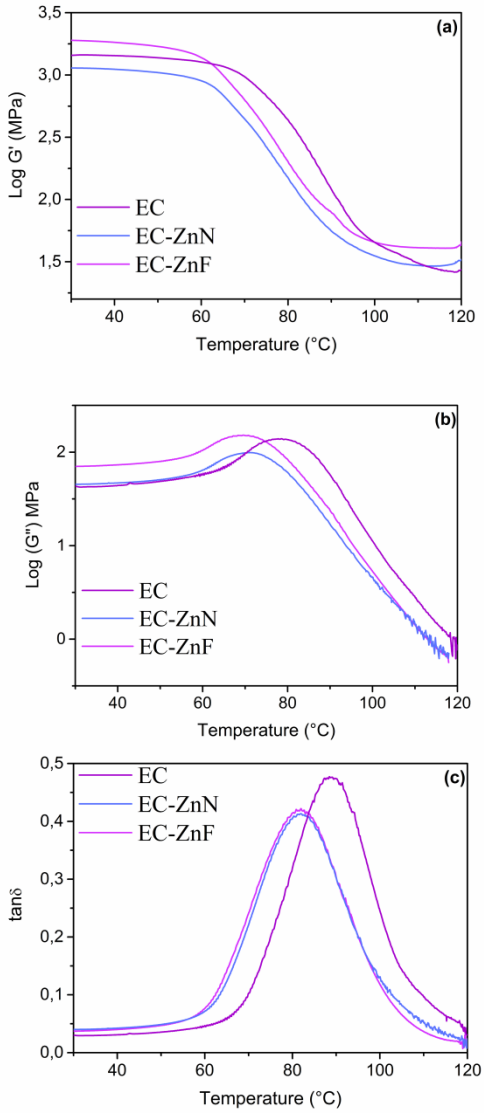

FIGURE 6. (a) Storage modulus, (b) loss modulus and (c) tanδ of ZnO composites.

The storage modulus G' (Figure 6a) of EC-ZnN nanocomposite is always lower than that of EC system. Conversely, in the case of EC-ZnF, the storage modulus is higher in both the glassy and rubbery state (plateau regions) with respect to the unfilled network. Figure 6c shows the tan δ curves for EC and its nanocomposites. The curves for EC-ZnF and EC-ZnN are similar, indicating that there are no differences in the dissipation of viscoelastic energy. However, EC peak position is shifted towards higher temperatures (Figure 6c), in accordance with the shape of the loss modulus in the same temperature range (Figure 6b). Besides, the curve reaches higher values in intensity. These differences are attributed to the different composition of the two UV-cured systems: in fact, EC nanocomposites contain a halved amount of CNC with respect to EC counterparts. CNC nanocrystals are likely to create voids within the polymer matrix, which are able to dissipate energy more efficiently. EC sample has higher amount of CNCs (4 wt.%), hence higher damping capacity as compared to EC-ZnF and EC-ZnN nanocomposites which embed 2 wt.% of CNCs. Tg values, estimated from the maximum of tanδ, are similar for EC nanocomposites (Tg= 82 °C) and are slightly lower with respect to EC (Tg=89 °C). Again, this difference can be ascribed to the different amount of CNCs. Finally, TG values obtained from DMTA analyses are higher as compared to those derived from DSC measurements: this difference is well documented in literature and is attributed to a frequency effect [27,28].

Assessment of the piezoelectric voltage generation by the synthesized composites

To verify the compatibility of EB/nanofillers couplings to generate a piezoelectric signal, open circuit voltage was quantified by integrating the synthesized materials in rectangular beam cantilever bonded to the shaker and connected to the DSO while a reference commercial accelerometer was used as sensor to measure the effective applied acceleration. When a mechanical stress is applied by means of the electromechanical shaker, the piezoelectric cantilever

is subjected to a strain; then a strain-induced electric polarization takes place. Consequently, opposite charges are accumulated on the Al electrodes (top and bottom side) and the piezoelectric potential is recorded by the DSO acquisition system. The oscillation of the beam causes an alternation of opposite strain, compressive and tensile. When the compressive strain is released, the accumulated charges return to the opposite direction, generating a reverse polarity, and the piezoelectric potential diminishes. By applying and releasing continuously the compressive stress, alternating voltages are generated. The piezoelectric response of the devices at their resonance frequency was measured in the time domain at different acceleration values (5 g, 7 g and 10 g). The generated open circuit voltages were determined as Root Mean Square (RMS) of the measured output signal and correlated to different experimental parameters, namely: i) fillers morphology, ii) deposition of AlN layer, iii) insertion of a proof mass.

Effect of ZnO needles/flowers nanofillers on the piezoelectric response of EC matrix

All the synthesized materials reveal a piezoelectric response, confirming the compatibility of the explored matrix-filler combinations. The resonance frequency of the prepared cantilevers (EC, EC-ZnN, EC-ZnF) was about 3.3 kHz. Table 2 collects the RMS output voltage generated by the as-deposited investigated samples at their resonance frequency.

Type of cantilever	**RMS output voltage (mV) at resonance frequency**		
	5g	7g	10g
EC	1.06±0.02	1.22±0.03	1.28±0.02
EC-ZnN	1.03±0.02	1.57±0.02	1.78±0.02
EC-ZnF	1.73±0.02	1.78±0.02	2.40±0.02

TABLE 2. RMS output voltage values of three analyzed samples at different acceleration values.

As expected, the generated output voltage increases with the applied acceleration. The contribution of CNC to voltage generation is quantifiable by the response of EC sample at different accelerations, as the pure acrylic matrix did not show any detectable piezoelectric response. The piezoelectric capability of the composite was enhanced replacing 2 wt.% of CNC with ZnO nanostructures. The composite containing ZnO flowers seems be the most promising, in terms of generated open circuit voltage, at different acceleration values.

Effect of the deposition of AlN layer on the piezoelectric response of the investigated samples

In order to investigate the impact of the proprietary growth of PVD AlN film [29] on the piezoelectric performance of the fabricated cantilevers, a 600 nm-thick AlN thin film was deposited by sputtering on the top side of the different cantilevers before depositing the Al electrode. This additional step on the comprehensive fabrication process is aimed at increasing the piezoelectric performance by the series-connection of the two piezoelectric layers. The characterization of the composites was performed by applying acceleration values of 5, 7 and 10 g on the rectangular cantilevers within a shaker vibration frequency range between 2.5 and 3.7 kHz, as reported in Figure 7.

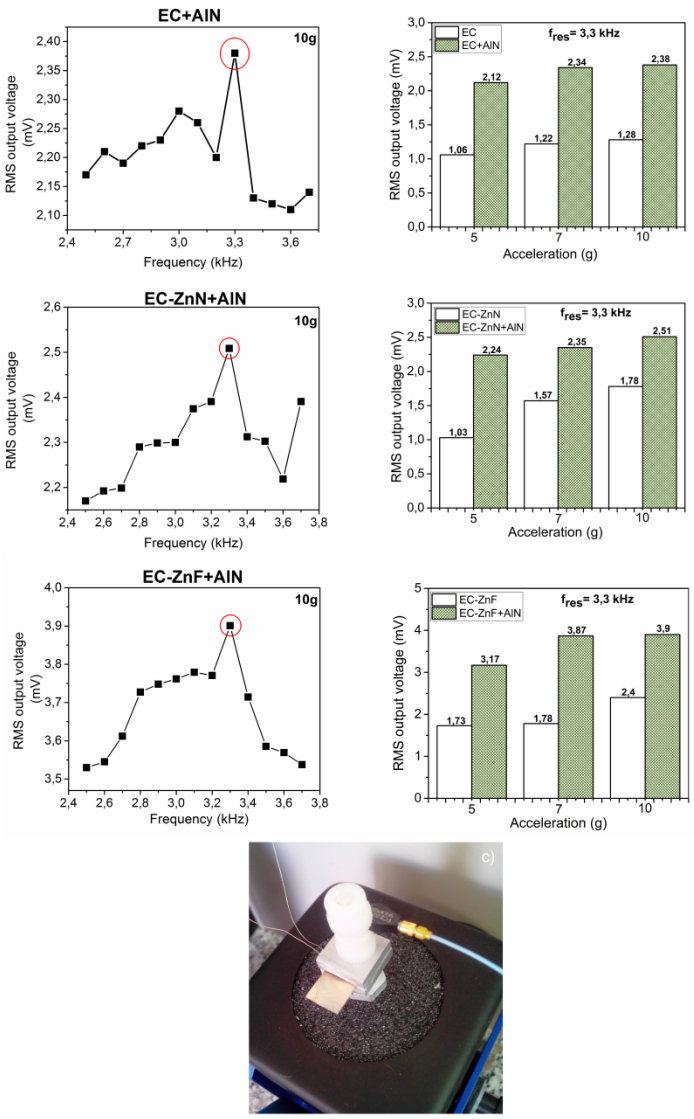

FIGURE 7. (a-left) voltage generated at 10 g acceleration for the analyzed samples covered by the AlN thin layer; (b-right) RMS open circuit voltage of all the characterized nanocomposite cantilevers, with and without AlN layer; (c-bottom) picture of a cantilever mounted on PCB 2007E shaker.

As indicated by the results shown in Figure 7a for representative samples characterized at 10 g of acceleration, the highest generation was confirmed at the resonance frequency of 3.3 kHz, the same found before the AlN deposition. This is reasonable, as the nitride film is very thin (600 nm thick), hence it does not affect the beam mass and the effective resonance frequency in a remarkable way. However, the addition of the nitride layer increases the harvested output voltage of all samples, as shown in Figure 7b, where the comparison of the two cases is depicted [30]. Figure 7c shows the fabricated cantilever mounted on PCB 2007E shaker for functional tests.

Further, as confirmed by the obtained results, a crystalline AlN piezoelectric film grows onto the EC matrix: its structural arrangement is favored by the presence of ZnO nanostructures incorporated in the matrix, while it is amorphous when the EB is unfilled (as shown in Figure 2). It is known that the piezoelectric activity of this nitride is mainly expressed along the perpendicular direction of the hexagonal structure or similarly along (0002) orientation. In this case, AlN grows along (100) and (101) planes on the nanocomposites, thus its piezoelectric contribution is lower than that expected, even if present [31]. However, being the AlN system far from the lowest energy state (due to the lack of (002) planes that have the lowest energy in the hexagonal system), the crystallization parameter could be tuned with the deposition parameters (being the deposition mainly a kinematically-limited process instead of an energy-limited one), in order to obtain (002) oriented nitride with a stronger piezoelectric response.

A simple explanation was formulated to interpret the observed results, with the help of Figure 8.

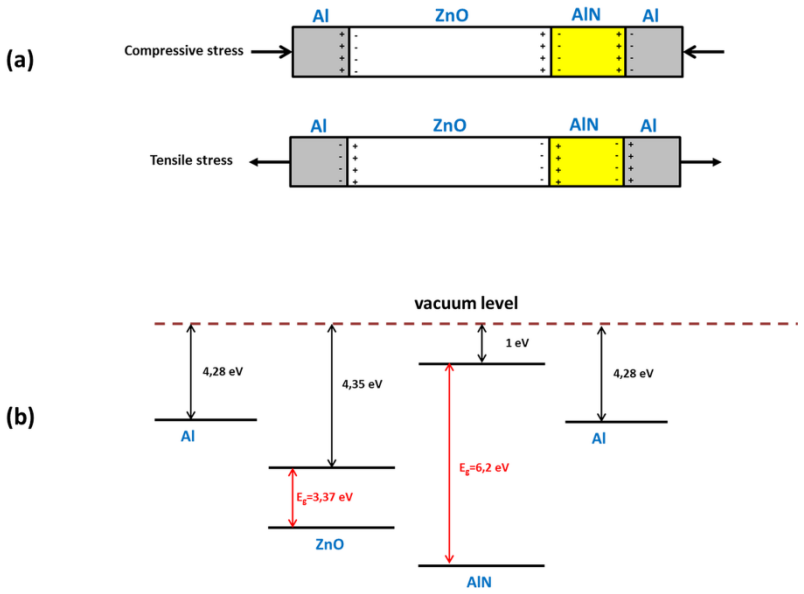

FIGURE 8. (a) Schematic charge distribution diagrams for the materials involved into the Al/(EB+ZnO)/AlN/Al stacked structure under a compressive force and under a tensile force and (b) diagram of their band alignment.

Being the AlN layer deposited only on one of the beam surfaces, the ZnO nanostructures, embedded in the acrylic network, have two types of interface, one coupled to the Al electrode

(ZnO/Al) and the other with the AlN layer (ZnO/AlN). When the stacked structure (Al_{bottom}/EB-NC-ZnO/AlN/Al_{top}) is mechanically excited, polarization occurs, as described previously. Thus, under compressive stress, the negative polarization charges generated from the ZnO internal structure will accumulate in the inner interface region of ZnO/Al, while the positive ones will accumulate in the inner interface region of ZnO/AlN (Fig. 8a). The established piezoelectric potential leads to an electrons flow from the Al electrode through the external circuit to the other Al electrode, generating a positive current. Similarly, when the successive tensile stress occurs, the accumulated positive and negative polarization charges will flow through the external circuit in the opposite direction. In this case, the presence of AlN interlayer between ZnO and Al electrode plays two roles that change the mechanism of the piezoelectric response of the stacked structure.

First, being a piezoelectric material, AlN adds an intrinsic contribution to the output signal coming from the beams. Second, due to its electronic band structure, AlN placed between ZnO and Al works like a high barrier to block the electrons leakage in a very effective way. The following considerations shed some light on this latter matter. The work function of Al is 4.28 eV, i.e. smaller than the electron affinity of ZnO, being approximately 4.35 eV [32], leading to an ohmic contact between them. When AlN interlayer is added, the contact state between ZnO and Al changes due to the small AlN electron affinity (about 1 eV) and the relatively high bandgap (6.20 eV). As a consequence, the leakage current caused by the ZnO internal structure can be effectively reduced to improve significantly the piezoelectric voltage (Fig. 8b).

Effect of the beam proof mass on the devices piezoelectric generation

A square-shaped iron tip mass of 0.55 g with a surface area of 25 mm^2, 0.5 mm thick was added to the free end of all the beams coated with the AlN layer, with the aim to increase the output voltage signal, thanks to a more effective applied strain. Besides, the tip mass shifts the resonance

frequency towards lower values. Figure 9 depicts the trend of the RMS output voltage at different accelerations close to the resonance frequency that is centered at 3 kHz (lower than 3.3 kHz without proof mass).

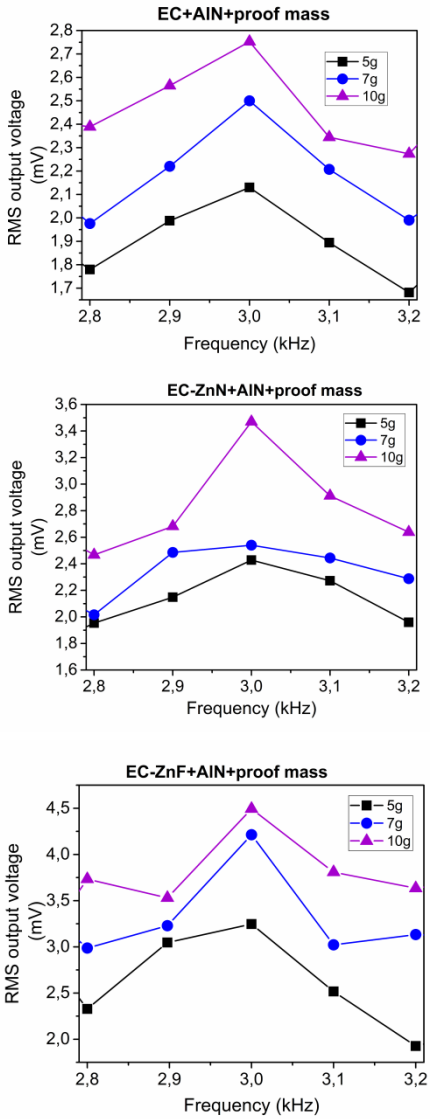

FIGURE 9. Output voltage of the beams at different g values with 0.55 g proof mass added at the beam tip.

The addition of the proof mass increases the RMS output voltage, as clearly shown in Figure 10. The average RMS output open circuit voltages of the investigated beams, reported in Figure 10, clearly show that the deposition of stacked AlN film on either unfilled EC or nanofillers-loaded EC, increases significantly the signal: this effect was more pronounced at lower acceleration (5 g) for

EC and EC-ZnN configurations. Higher voltage differences with proof mass insertion were measured in the EC-ZnF sample at low/medium accelerations (5 g and 7 g), while at 10 g a smaller signal enhancement was recorded. The best efficiency, in terms of generated RMS open circuit voltage normalized to the acceleration value (mV_{RMS} /g_{max}), was obtained by the EC-ZnF-AlN based beams at 5 g and with proof mass, with a value of 0.650 mV/g vs. 0.635 mV/g obtained for the EC-ZnF-AlN blend, at 5 g and without proof mass.

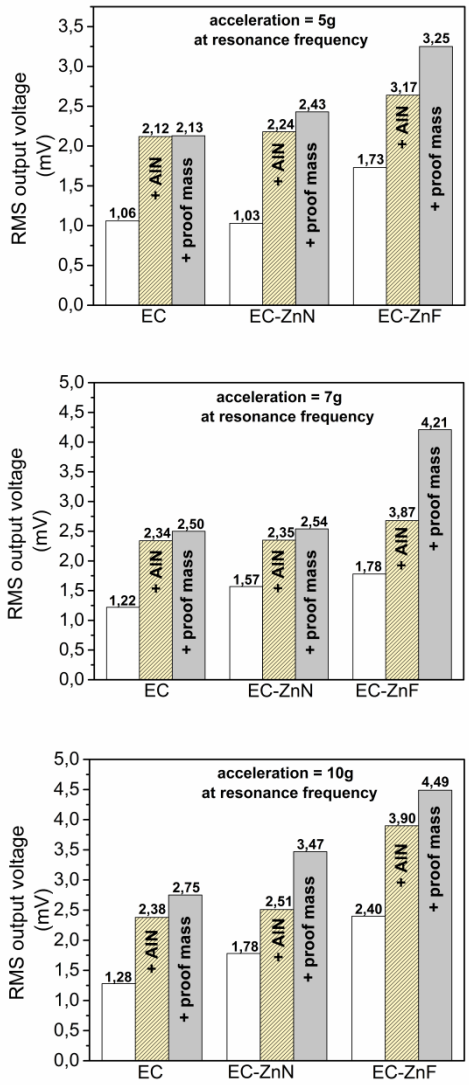

FIGURE 10. RMS output voltage values obtained by different beams configurations.

Characterization of the electric contacts: resistivity measurements

In order to optimize the beams energy harvesting capabilities, the voltage drop at the piezoelectric film/contact interface is crucial and heavily affects the generated power. Low contact resistance is one of the most desirable properties of metal contacts on piezoelectric generators; in this work, the sheet resistance of Al contacts was measured by using a four-point cylindrical probe approach. The four-point probe (from Jandel Engineering) consists of a linear array of four 1 mm spaced probe needles made of tungsten carbide. The current flows through the two outer probes and the potential is measured between the two inner probes. The sheet resistance of Al thin films increases from 1.4-1.5 Ω/□ to 18-23 Ω/□ when the Al contact is deposited on AlN thin film. The obtained results demonstrate that metal contacts deposited on the nitride film show a higher electrical resistivity than those on the piezoelectric resin. This finding could be ascribed to the structure and morphology of the deposited AlN layer, which results affected by the composition of the underlying UV-cured substrate. As a consequence, the electrical properties of the surface electrode change. Further optimizations of the electrical contacts onto AlN film will be beneficial for limiting the voltage drop at the contact interface. In addition, a more accurate interpretation of the obtained results requires to consider other sources causing the attenuation of the generated voltage, not strictly connected to the deposition process, such as electronics interference, leakage current, etc.

SUMMARY AND CONCLUSIONS

This work deals with the synthesis and characterization of composites, based on as-deposited zinc oxide (ZnO) nanostructures (namely, flowers or needles) and cellulose nanocrystals dispersed in a UV-curable acrylic system, to verify the compatibility of the materials couplings for potential

applications in the field of functional coatings or self-powered devices. The loading of piezoelectric fillers (only CNC or CNC with ZnO needles or flowers) was kept constant at 4 wt.%. All the systems were fully cured in the adopted experimental conditions, as assessed by DSC analyses. Moreover, whatever the fillers morphology is, the thermal stability of EC-ZnO nanocomposites is not significantly different to that of EC. Conversely, the T_{max} of the last degradation step is slightly higher than that of EC film. Rectangular beams were fabricated by using the nanocomposites as active material for piezoelectric devices and the RMS output open circuit voltage was evaluated with three different accelerations (5, 7 and 10 g) at their resonance frequency (3.3 kHz), irrespective of the morphology of the nanostructures. The addition of a sputtered AlN layer on one side of the beam was also investigated, aiming at improving the piezoelectric voltage generation. The presence of the nitride layer increased the RMS open circuit output voltage from values in the range 1-2.4 mV up to 3.9 mV (obtained for flowers ZnO nanostructures), while the resonance frequency remained unchanged. The tuning of the resonance frequency and output voltage enhancement were tested by inserting a proof mass on the tip of the rectangular structures. In this case, the resonance was lowered down to 3 kHz and the open circuit output voltage was further increased up to 4.5 mV for EC-ZnF+AlN sample. At all the investigated accelerations, ZnO nanoflowers provide the highest output signal and efficiency, in terms of generated RMS open circuit voltage normalized to the acceleration value (mV_{RMS} /g_{max}): the best efficiency was obtained by the EC-ZnF-AlN based beams at 5 g and with proof mass, with a value of 0.65 mV/g versus 0.635 mV/g obtained for the EC-ZnF-AlN blend yet, at 5 g and without proof mass.

In conclusion, a simple and cost effective fabrication was proposed to develop vibrational systems, which could be competitive in the field of green energy generation. As initial approach, as-synthesized ZnO nanostructures have been dispersed into acrylic matrix. Once assessed the piezoelectric response of the investigated nanocomposites, future research will be focused

towards the optimization of the active material to maximize its efficiency, first by obtaining well oriented and uniformly dispersed ZnO nanostructures within the acrylic matrix. Moreover, further efforts will be aimed to the tuning of the resonance frequency to harvest energy at low frequency from environmental vibrations.

Conflict of interest

The author(s) declare no competing interests.

Author contributions

M.A.S., C.D.P., D.D.,G.M, L.F.: Conceptualization, Formal analysis, Methodology, Data curation, Writing-Original draft preparation. C.D.P. and L.F.: Software, Validation. G.M., A.F. and D.D.: Investigation, Data curation, Validation. L.F. and P.S.: Supervision. M.A.S., L.F., M.M, E.M. M.C.M.: Investigation, Validation.

REFERENCES

[1] Eslamian, M. *Prog. Org. Coat.* **2017**, *113*, 60–73.

[2] Teck Chye Ang, D., Kum Khong, Y., Neon Gan, S. *Prog. Org. Coat.* **2013**, *76*, 705-711.

[3] Yildiz, F. *J. Technol. Studies* **2009**, *35*, 40–48.

[4] Vladu, M. I., Głowacki, E. D., Voss, G., Bauer, S., Serdar Sariciftci, N. *Mater. Today* **2012**, *15*, 340–346.

[5] Zhang, G., Zhao, P., Zhang, X., Han, K., Zhao, T., Zhang, Y., Jeong, C.K., Jiang, S., Zhang, S., Wang, Q. *Energy Environ. Sci.* **2018**, *11*, 2046-2056.

[6] Saleh, E., Woolliams, P., Clarke, B., Gregory, A., Greedy, S., Smartt, C., Wildman, R., Ashcroft, I., Hague, R., Dickens, P., Tuck, C. *Addit. Manuf.* **2017**, *12*, 143-148.

[7] Decker, C. *Polym. Int.* **1998**, *45*, 133-141.

[8] Banerjee, S., Cook-Chennault, K.A. *Composites Part A: Applied Science and Manufacturing* **2012**, *43*, 1612–1619.

[9] Yadav K., Smelser, C.W., Jacob, S., Blanchetiere, C., Callender, C.L., Albert, J. *Appl. Phys. Lett.* **2011**, *99,* 031109.

[10] Banerjee, S., Cook-Chennault, K.A., Du, W., Sundar, U., Halim, H., Tang, A. *Smart Mater. Struct.* **2016**, *25*, 115018.

[11] Ferrone, E., Araneo, R., Notargiacomo, A., Pea, M., Rinaldi, A. *Nanomater.* **2019,** *9*, 1449.

[12] Mahadeva, S.K., Walus, K., Stoeber, B. *ACS Appl. Mater. Interfaces* **2014**, *6,* 7547–7553.

[13] Nowak, M., Tanski, T., Szperlich, P., Matysiak, W., Kepinska, M., Stroz, D., Bober, Ł., Toron, B. *Ultrason. Sonochem.* **2017**, *38*, 544–552.

[14] Banerjee, S., Du, W., Sundar, U., Cook-Chennault, K.A. *J. Nanomater.* **2018**, *2018*, 6939621.

[15] Singh, P.K., Gaur, M.S., Johari, D., Sagar, R., Gupta, A., Sharma, A., Singh, G., Yadav, M. *Thin Solid Films* **2019**, *682*, 121–125.

[16] Cataldi, A., Esposito Corcione, C., Frigione, M., Pegoretti, A., *Prog. Org. Coat.* **2017**, *106*, 128–136.

[17] Grishkewich, N., Mohammed, N., Tang, J., Tam, K. C. *Curr. Opin. Colloid Interface Sci.* **2017**, *29*, 32-45.

[18] Csoka, L., Hoeger, I. C., Rojas, O. J., Peszlen, I., Pawlak, J. J., Peralta, P. N. *ACS Macro Lett.* **2012**, *1*, 867−870.

[19] Fan, F. R., Tang, W., Wang, Z. L. *Adv. Mater.* **2016**, *28*, 4283-305.

[20] Kim, J. H., Ko, H.U. (Thereof.). US Patent 9, 698, 336, 2012.

[21] Kumar, A., Gullapalli, H., Balakrishnan, K., Botello-Mendez, A., Vajtai, R., Terrones, M., Ajayan, P. M. *Small* **2011**, *7*, 2173-8.

[22] Li, C., Xie, Y., Liu, Q., Zheng, Y., Zhang, X., Dong, W. *Fibers and Polymers* **2014**, *15*, 281-285.

[23] Suja, M., Bashar, S.B., Debnath, B., Su, L., Shi, W., Lake, R., Liu, J. *Sci. Rep.* **2017**, *7,* 2677.

[24] Malucelli, G., Fioravanti, A., Francioso, L., De Pascali, C., Signore, M. A., Carotta, M. C., Bonanno, A., Duraccio, D. *Prog. Org. Coat.* **2017**, *109*, 45–54.

[25] Sauperl, O., Stana-Kleinschek, K., Ribitsch, V. *Text. Res. J.* **2009**, *79*, 780-791.

[26] Dorigato, A., Pegoretti, A., Dzenis, Y. *Mech. Mater.* **2013**, *61*, 79-90.

[27] Nielsen, L. E.; Landel, R. F. In *Mechanical Properties of Polymers and Composites*, Marcel Dekker, New York , **1994**.

[28] Allen, G. M., Drain, K. F. *Radiation Curing of Polymeric Materials*, ACS Symposium Series No. 417, Washington, **1990**, p. 242.

[29] Signore, M. A., Taurino, A., Catalano, M., Kim, M., Che, Z., Quaranta, F., Siciliano, P. *Mater. Des.* **2017**, *119*, 151-158.

[30] Zhu, L. Y., Yang, J. G., Yuan, K., Chen, H. Y., Wang, T., Ma, H. P., Huang, W., Lu, H. L., Zhang, D. W. *APL Mater.* **2018**, *6*, 121109-3.

[31] Shang, Z. G., Li, D. L., Wen, Z. Y., Zhao, X. Q. *Key Eng. Mater.* **2013**, *562-565*, 942-946.

[32] Alivov, Y. I., Kalinina, E. V., Cherenkov, A. E., Look, D. C., Ataev, B. M., Omaev, A. K., Chukichev, M. V., Bagnall, D. M. *Appl. Phys. Lett.* **2003**, *83*, 4719-4721.